Proceedings of Global Power and Propulsion Society
ISSN-Nr: 2504-4400
GPPS Xi'an21
18th–20th October, 2021

www.gpps.global

GPPS-TC-2021-0168

Performance Impact of Uncertain Variations of Inlet Flow for Axial Compressor Blades

Zeshuai Chen
Zhejiang University
zeshuai.chen@zju.edu.cn
Hangzhou, Zhejiang, China

Jiaqi Luo
Zhejiang University
jiaqil@zju.edu.cn
Hangzhou, Zhejiang, China

Yalu Zhu
Zhejiang University
zhuyalu2010@163.com
Hangzhou, Zhejiang, China

Zhiheng Xia
China Aerodynamics Research and Development Center
xiazhiheng@cardc.cn
Mianyang, Sichuan, China

ABSTRACT

The impact of inlet flow variations on turbomachinery flow is common in the real world, resulting in undesirable performance deteriorations in engineering. The origin of performance changes and how to evaluate the changes require to be studied, which is of high significance in both academic and engineering communities. On use of CFD and the non-intrusive polynomial chaos (NIPC) method, performance impact considering the stochastic variations of inlet flow angle for a transonic compressor rotor blade is studied in the paper. A detailed grid-independent study assisted by Richardson extrapolation is firstly presented to illustrate the reliability of CFD solutions. Then the implementations of NIPC employing adaptive sparse grid are introduced. Performance uncertainty quantification of NASA Rotor 67 is evaluated using NIPC and the effects of different distributions of inlet flow angle variation (IFAV), different ranges of IFAV on the performance changes at different operation conditions are presented. Finally, statistical analysis on flow solutions by Monte Carlo simulation is performed. The adiabatic efficiency along span at the outlet and the flow solutions in the blade passage are presented and discussed to demonstrate the impact mechanisms of IFAV.

1. Introduction

Over the past few decades, highly optimized blades and efficient compression system had been designed benefiting from the advanced numerical methods in terms of computational fluid dynamics (CFD) and design optimization (Ju and Zhang, 2010). Besides performance improvements, robust design considering the effects of uncertainties has attracted wide attention in recent years because the performance dispersity can be reduced through robust design. Thus, uncertainty quantification (UQ) for evaluating performance impact has become an important module of robust design. For example, realistic compressor blades inevitably exhibit geometric variations due to manufacturing variability, fouling, corrosion, etc. (Diakunchak, 1992). Moreover, the geometric variations near leading edge subsequently induce inlet flow angle variation (IFAV).

In the 1970s, Bammert et al. (Bammert and Sandstede, 1976) successfully quantified the influence of geometric variations on the performance of a turbine by experimental measurements on the thinned and thickened blades. At the beginning of this century, By the direct Monte Carlo simulations (MCS), Garzon et al. (Garzon and Darmofal, 2003) successfully evaluated the impact of geometric variability on the aerodynamic performance of compressor blades, releasing the researchers from time-consuming and high-cost experiments. Edwards et al. (Edwards et al., 2011) numerically investigated the influence of blade geometric variations on the aerodynamic performance of a transonic nozzle guide vane. Generally, using the direct MCS, usually a large number of samples are necessary. The computational cost is considerable, especially for the studies involving three-dimensional flow computations.

For reducing the computational cost, surrogate model methods rather than the direct MCS have been in use. Loeven et al. (Loeven et al., 2007) introduced a non-intrusive probabilistic collocation method, which was then demonstrated through the study of performance impact of uncertain free stream velocity for NACA0012 airfoil. Gopinathrao et al. (Gopinathrao

et al., 2009) successfully investigated the impact of different uncertainties on the aerodynamic performance of NASA Rotor 37 by using a non-intrusive polynomial chaos (NIPC). Loeven et al. (Loeven and Bijl, 2010) employed the probabilistic collocation method to quantify the performance impact of uncertain inlet total pressure profile for NASA Rotor 37. They illustrated that the flow near the shock wave exhibits the most intensified variations, especially on the outer spans. Qin et al. (Qin et al., 2016) quantified the performance variations of a cascade by using a dimension reduction technique. Li et al. (Li et al., 2018) quantified the performance impact of a transonic axial compressor using NIPC and ranked the uncertainties of inlet total pressure, inlet turbulence intensity, surface roughness, endwall roughness, blade thickness and tip clearance size according to the performance changes. Xia et al. (Xia et al., 2019) quantified the variations of adiabatic efficiency and mass flow rate of NASA Rotor 67 considering the effects of inlet total pressure and outlet back pressure variations by using NIPC.

Generally, polynomial chaos has been widely applied to uncertainty studies, especially for the problems with large-scale uncertainties, i.e., the sensitivity analysis based evaluations (Luo and Liu, 2018) are inaccurate. Due to its easy implementation, NIPC has become the most welcomed surrogate model method for UQ studies. Besides, although a few open literature has quantified the impact of different uncertainties on the aerodynamic performance of transonic compressor rotor blades, the mechanisms of performance variations due to the uncertainties have not been well demonstrated.

The present study will investigate the impact of IFAV on a transonic compressor rotor blade, NASA Rotor 67 by NIPC. A detailed grid-independent study assisted by Richardson extrapolation (RE) is firstly presented to illustrate the reliability of CFD solutions. Then an adaptive sparse grid sampling technique is used to generate the training samples for NIPC to reduce the computational cost needed by model construction. The effects of IFAV at different operation conditions on the relative variations of adiabatic efficiency (RVAE) are illustrated and discussed in detail. Finally, statistical flow solutions obtained by the direct MCS are presented to demonstrate the impact mechanisms of IFAV on the typical flow of transonic compressor rotor blade, including flow separation, shock wave and tip-leakage flow.

2. Flow validation

NASA Rotor 67 is the rotor of the first stage of a two-stage axial compressor. It was designed in 1970s and then experimentally studied by Strazisar et al. (Strazisar et al., 1989). It has 22 blades with an aspect ratio of 1.56. The total pressure ratio and mass flow rate at the design condition are 1.63 and 33.25 kg/s, respectively. The design rotational speed is 16,043 rpm with a tip speed of 429 m/s. The tip clearance is about 1.0 mm. The experimental results provided by Strazisar et al. (Strazisar et al., 1989) are used in the study for CFD verification and validation.

Table 1 Grids of numerical simulations

N	1	2	3	4
N_0	2.7×10^6	1.8×10^6	1.2×10^6	0.8×10^6
N_{tip}	65	49	33	17
π	1.6127	1.6127	1.6129	1.6155
π_{RE1}		1.61265		–
π_{RE2}	–		1.61268	

The Reynolds-averaged Navier-Stokes (RANS) equations and the Spalart-Allmaras turbulence model equation (Spalart and Allmaras, 1992) are solved on multi-block grids using an in-house program. Roe scheme and multi-grid acceleration technique are used. The flow solutions are evolved by the LU-SGS implicit time-marching. The given total pressure, total temperature and flow angle at the inlet are 101315 Pa, 288.15 K and zero degree, respectively. The back pressure is given on the hub at the outlet and the spanwise distribution of static pressure is determined by radial equilibrium method.

Four grids are used in the study on grid convergence, the resolutions of which are given in Table 1, where N_0 and N_{tip} are the approximate cell number and the spanwise grid number in the tip gap, respectively. Besides, the computed total pressure ratio, π of each grid as well as the RE results are also presented in the table. π_{RE1} and π_{RE2} are the RE results obtained from the former and latter three grids, respectively. The evolutions of grid convergence are presented in Fig. 1(a). The results of Grid 2 and Grid 1 are pretty close to the RE solution, which are usually regarded as the approximate exact one. In the following study, Grid 2 is employed. The overall performance parameters, π and adiabatic efficiency, η of Rotor 67 calculated on Grid 2 are given and compared with the experimental ones in Fig. 1(b). It should be mentioned that the mass flow rate is normalized by the choked value. Compared with the experiment, the computed total pressure ratio is a little lower, while the adiabatic efficiency exhibits good agreements.

3. Uncertainty quantification

The Gaussian and uniform distributions have been widely used in academic research (Hosder et al., 2007), which are used in the study to describe the uncertain variations of inlet flow angle. Especially, the Gaussian distribution has been recognized and widely used for most natural random events. Therefore, the variation of inlet flow angle is assumed in the

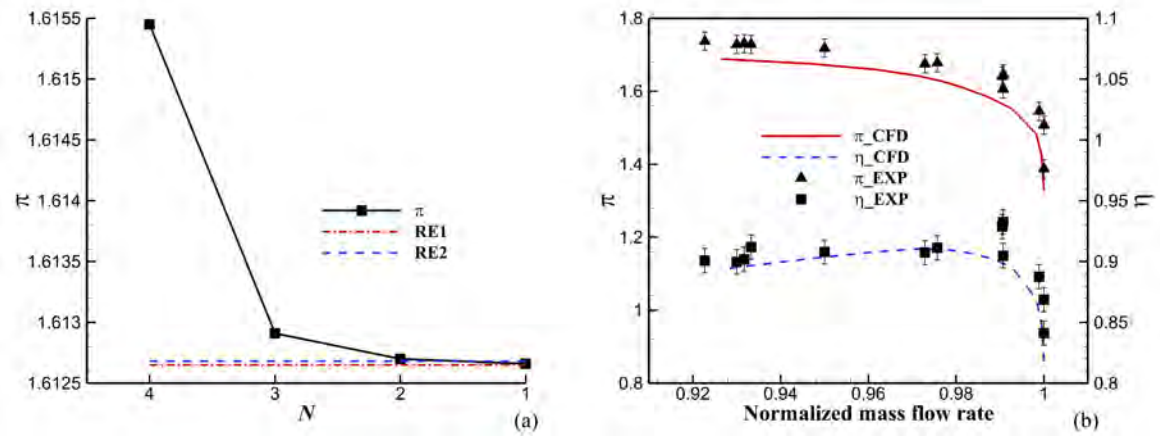

Figure 1 (a) Grid-independence of total pressure ratio; (b) Comparisons of operation characteristics of Rotor 67

study to agree the distribution as follows.

$$f(\xi) = \begin{cases} \frac{1}{\sqrt{2\pi}} \exp\left(-\frac{\xi^2}{2}\right), & \xi \in [-E, E] \\ 0, & \text{otherwise} \end{cases} \tag{1}$$

where $E = 2.0$, ξ is defined by

$$\xi = \frac{\alpha - \alpha_{ref}}{\sigma_\alpha} \tag{2}$$

α and α_{ref} are the perturbed and reference inlet flow angle, respectively, σ_α is the standard deviation (Std) of IFAV. In the study, $\alpha_{ref} = 0°$ and $\sigma_\alpha = 5°$.

3.1 Adaptive sparse grid

Sparse grid technique starts from one-dimensional interpolation. Assume that we want to approximate smooth function $f \to \mathbb{R}$, we have

$$\mathscr{U}^i(f) = \sum_{j=1}^{m_i} f\left(x_j^i\right) \cdot a_j^i \tag{3}$$

where x_j^i, m_i and a_j^i are the interpolation points, the number of interpolation points and the basis functions such as Lagrange polynomials, respectively. While in the multidimensional problems with $d > 1$, the interpolation formula defined as tensor product can be written as

$$\left(\mathscr{U}^{i_1} \otimes \cdots \otimes \mathscr{U}^{i_d}\right) = \sum_{j_1=1}^{m_{i_1}} \cdots \sum_{j_d=1}^{m_{i_d}} f\left(x_{j_1}^{i_1}, \cdots, x_{j_d}^{i_d}\right) \cdot \left(a_{j_1}^{i_1} \otimes \cdots \otimes a_{j_d}^{i_d}\right) \tag{4}$$

which serve as building blocks for the Smolyak algorithm (Smolyak, 1963). Obviously, the above product formula needs $m_{i_1} \cdots m_{i_d}$ function values to construct a grid.

The Smolyak formulas $\mathscr{A}(q,d)$ are linear combinations of product formulas with the following two properties. First, only products with a Relatively small number of knots are used. Second, the interpolation property for $d = 1$ is preserved when $d > 1$. For $i \in \mathbb{N}$, with $\mathscr{U}^0 = 0$, define $\Delta^i = \mathscr{U}^i - \mathscr{U}^{i-1}$. Moreover, we put $|\mathbf{i}| = i_1 + \cdots + i_d$ for $\mathbf{i} \in \mathbb{N}^i$. For k-level sparse grid interpolation of f, where $q = k + d$, is then give as (Xiong et al., 2009)

$$\mathscr{A}(q,d)(f) = \sum_{k+1 \le |\mathbf{i}| \le q} (-1)^{q-|\mathbf{i}|} \cdot \begin{pmatrix} d-1 \\ q-|\mathbf{i}| \end{pmatrix} \cdot \left(\mathscr{U}^{i_1} \otimes \cdots \otimes \mathscr{U}^{i_d}\right)(f) \tag{5}$$

where $k = |\mathbf{i}| - d$. To compute $\mathscr{A}(q,d)(f)$, one only needs to know function values at the sparse grid

$$\mathscr{H} = \bigcup_{k+1 \le |\mathbf{i}| \le q} \left(\mathscr{X}_{i_1} \times \cdots \times \mathscr{X}_{i_d}\right) \tag{6}$$

where $\mathscr{X}_i = \left\{x_1^i, \cdots, x_{m_i}^i\right\}$ denotes the set of points used by $\mathscr{U}^i$. For $d = 1$, the formula can be simplified as $\mathscr{H} = \bigcup_{k+1 \le |\mathbf{i}| \le q} (\mathscr{X}_{i_1})$. Generally, we prefer to use nested grid, the Newton-Cotes grid and piecewise linear basis functions are employed in sparse grid in the study. (Gerstner and Griebel, 1998)

Since the principles of sparse grid are conceptually introduced above, to construct the adaptive sparse grid, we define the hierarchical surplus (HS) on the k-th grid level

$$w_{\mathbf{j}}^{k,\mathbf{i}} = f\left(x_{\mathbf{j}}^{\mathbf{i}}\right) - \mathscr{A}(k+d-1,d)\left(x_{\mathbf{j}}^{\mathbf{i}}\right) \tag{7}$$

where **j** denotes the number of basis points on the k-th grid level. As k increases to infinity, w tends to zero for continuous functions. Thus, HS can be used to evaluate the error tolerances ε in the adaptive sparse grid. The procedure of adaptive sparse grid have already been introduced in previous work (Xia et al., 2019). It is not presented in the study herein.

To illustrate the evolutions of adaptive sparse grids, Fig. 2 gives the distributions of the grids produced on each level at the operation conditions near peak efficiency (PE) and near stall (NS), where ANIPC indicates adaptive NIPC introduced in the following section. Starting from the third level, more and more grids are dynamically produced in the range [−10°, 10°], especially in the range where the adiabatic efficiency exhibits significant changes versus the inlet flow angle. The results demonstrate that the proposed adaptive sparse grid works effectively.

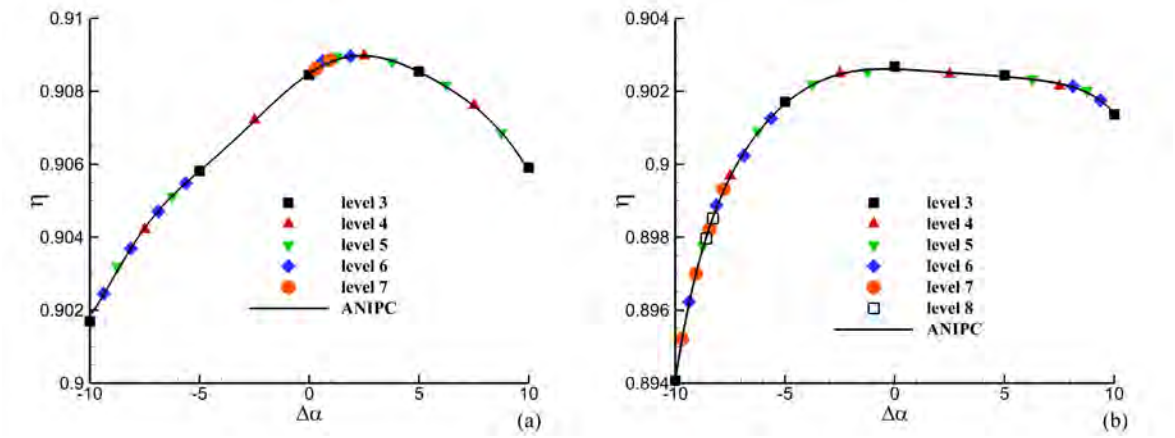

Figure 2 Grid evolutions of the adaptive sparse grid with tolerance ε = 1.0E-04: a) PE; b) NS.

3.2 Adaptive non-intrusive polynomial chaos

If the Std of a random process exists and has a finite value, it is said that the random process is second-order. A general second-order random process $X(\theta)$, described as a function of a random event θ, can be given as following formula.

$$X(\theta) = \sum_{j=0}^{\infty} u_j \Psi_j(\xi(\theta)) \tag{8}$$

where $\Psi_j(\xi)$ is random basis function corresponding to the j-th mode, the coefficients u_j is the amplitude of the j-th mode. In NIPC method , different randomly distributed events correspond to different polynomial chaotic basis functions. As the inlet flow angle variations are assumed to agree Gaussian distribution, Hermite polynomials are used as the basis function is the present study.

In actual application, the sum of the former P terms of the equation 8 is usually used to approximate $X(\theta)$ by the truncation theory.

$$X(\theta) \approx \sum_{j=0}^{P} u_j \Psi_j(\xi), \quad P = \frac{(n+p)!}{n!p!} - 1 \tag{9}$$

Exponential convergence of the above equation versus p can be obtained if the random process X share the same probability density with ξ. (Boyd, 1980) Thus, orthogonality of the NIPC basis in the L_2 space of Gaussian random variables enables the evaluation of the truncated NIPC representation by projecting the random process onto the NIPC basis.

$$u_j = \frac{\langle X\Psi_j \rangle}{\left\langle \Psi_j^2 \right\rangle} \tag{10}$$

In the present study, the coefficients of the ANIPC is calculated by Galerkin projection combined with the adaptive sparse grid technique. Once the adaptive model is constructed, the response results can be obtained effectively.

3.3 Performance impact evaluation

In order to assess the response performance of ANIPC including response accuracy and model training cost, RVAE at the operation conditions near PE and NS of Rotor 67 are statistically evaluated. By using ANIPC, the adiabatic efficiency can be calculated by

$$\eta = \sum_{i=0}^{p} a_i H_i(\Delta\alpha) \tag{11}$$

where $p = 8$, H_i are Hermite polynomial chaos. The error tolerance ε of sparse grid are $1.0E-4$ and $1.0E-3$ at PE and NS, respectively. The mean response error ε_{avr} and the deviation of response error, ε_{std} of ANIPC are defined as

$$\varepsilon_{avr} = \frac{1}{M}\sum_{i=1}^{M} |\eta_{NIPC} - \eta_{CFD}| / \eta_{CFD}, \quad \varepsilon_{std}^2 = \frac{1}{M-1}\sum_{i=1}^{M} (\delta_\eta - \varepsilon_{avr})^2 \tag{12}$$

where η_{NIPC} and η_{CFD} are the performance functions obtained by ANIPC and CFD, respectively, δ_η is the absolute value of RVAE, M is the number of test samples.

Table 2 Statistics of RVAE and response error of ANIPC

	Case A	Case B	Case C	Case D
$\mu_{\Delta\eta}/\%$	-0.104	-0.114	-6.936E-02	-7.062E-02
$\sigma_{\Delta\eta}$	1.684E-03	1.749E-03	1.242E-03	1.275E-03
$\varepsilon_{avr}/\%$	6.04E-03	1.27E-02	3.31E-03	9.10E-03
ε_{std}	4.26E-05	1.12E-04	2.50E-05	8.22E-05
N	23	7	27	9
ε	1.0E-04	1.0E-03	1.0E-04	1.0E-03

Table 2 gives the statistical results of RVAE and the response performance of ANIPC at PE and NS. Moreover, the results with different error tolerance are given and compared. The results of Case A and Case B are the ones at PE, while those of Case C and Case D are the ones at NS. A large number of 80,000 random statistical samples agreeing Gaussian distribution are used for statistical analysis. In the table, N is the number of sparse grids used for model construction of ANIPC, $\mu_{\Delta\eta}$ and $\sigma_{\Delta\eta}$ are the statistical mean and Std of RVAE, respectively. It can be found that with a lower error tolerance, ε, more sparse grids are necessary for constructing NIPC model with satisfied response accuracy. Moreover, compared with Case A, the statistical mean and Std of Case C are dramatically lower, implying that the adiabatic efficiency of Case A suffers more intensified uncertainty impact of IFAV. As shown in Fig. 2, the adiabatic efficiency at NS is insensitive to IFAV in a wider range, which is responsible for the lower statistical mean and Std as shown in Table 2.

Besides, the effects of uncertainty distribution of IFAV, $\Delta\alpha$ on performance changes of Rotor 67 are also investigated. From now on, the variation of inlet flow angle is assumed to agree the following uniform distribution.

$$f(\xi) = \begin{cases} \frac{1}{2E}, & \xi \in [-E, E] \\ 0, & \text{otherwise} \end{cases} \tag{13}$$

Table 3 Statistics with different distributions of IFAV

	Norm_{PE}	Unif_{PE}	Norm_{NS}	Unif_{NS}
$\mu_{\Delta\eta}/\%$	-0.104	-0.173	-6.936E-02	-0.128
$\sigma_{\Delta\eta}$	1.684E-03	2.096E-03	1.242E-03	1.937E-03

The same statistical samples are used. The statistical results of uniform and Gaussian distributions are given in Table 3. In the table, Norm and Unif represent Gaussian and uniform distribution, respectively, the subscripts PE and NS are the operation conditions. It is clear that the statistics of uniform distribution are larger than those of Gaussian distribution at PE and NS.

Figure 3 presents the probability density function (PDF) and cumulative density function (CDF) of RVAE with different distributions of IFAV at PE and NS. From the figure, it can be found that the PDFs of RVAE completely deviate from the given distributions of IFAV, indicating that the adiabatic efficiency is strongly nonlinear dependent on IFAV at both PE and NS. Moreover, when the variation of inlet flow angle agrees Gaussian distribution, the statistical samples are more concentrated. Subsequently, the variations of adiabatic efficiency are also more concentrated, resulting in lower statistical mean and Std, which can be confirmed by CDFs. As shown in Fig. 3, the CDF of Gaussian distribution increases slower

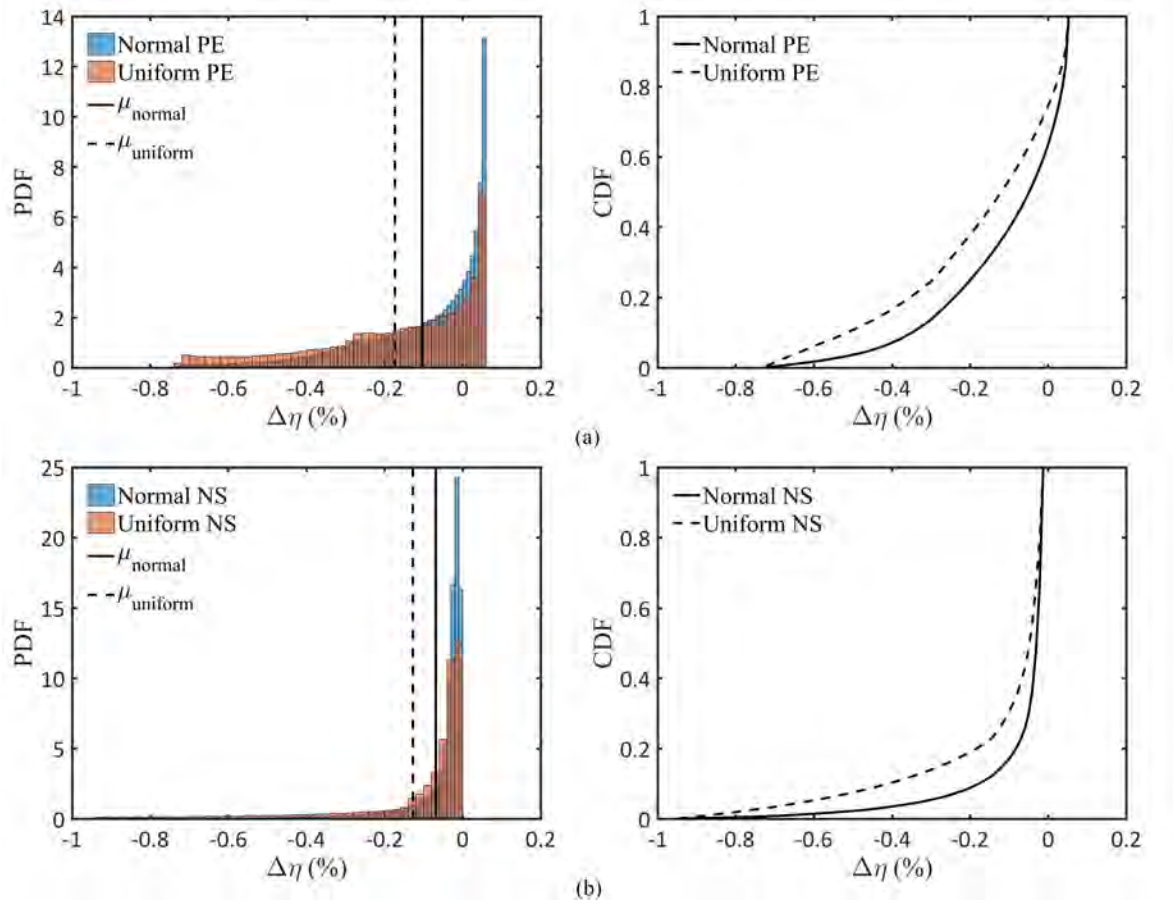

Figure 3 PDFs and CDFs of RVAE with different distributions of IFAV at the operation conditions: a) PE; b) NS.

than that of uniform distribution at both PE and NS. Furthermore, compared with the PDFs at PE, the PDFs of RVAE at NS are more concentrated. That's why the statistics at NS are lower than those at PE as shown in Table 2.

Moreover, the effects of the range in which the inlet flow angle varies on RVAE are investigated. Figure 4 gives the statistics of RVAE for five different ranges of IFAV, i.e., [−2°, 2°], [−4°, 4°], [−6°, 6°], [−8°, 8°] and [−10°, 10°]. It can be found that the mean performance change and Std increases as the range of IFAV increases. It is interesting that although the statistics at PE are higher than those at NS, the statistics at PE exhibit almost linear dependence on the range of IFAV. However, the statistics at NS exhibit approximate quadratic variations versus the range of IFAV.

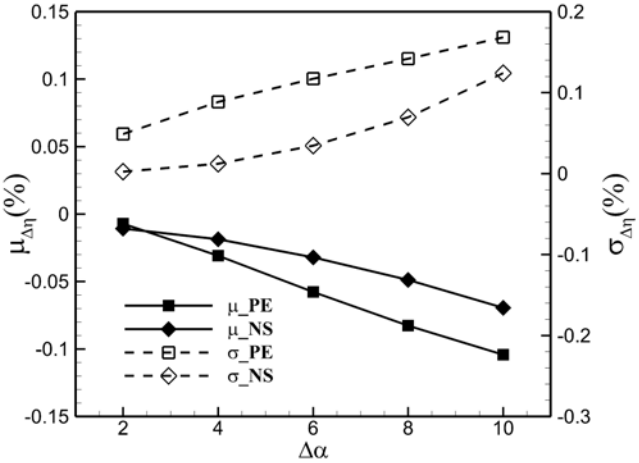

Figure 4 Statistics of RVAE versus the range of IFAV

4. Statistical analysis of flow solutions

In the aforementioned section, the adiabatic efficiency changes at different operation conditions have been quantified with different ranges and different distributions of IFAV. However, it is still not clear how the IFAV affect the RVAE. In this section, the direct MCS with 100 random samples agreeing the Gaussian distribution is employed to explore the impact mechanisms of IFAV. The literature (Xia et al., 2019) showed that the convergence of MCS is usually slow and thousands of statistical samples are necessary. Although the direct MCS with only 100 samples is unable to determine the converged results, it can still be used to qualitatively reveal the mechanisms of performance impact.

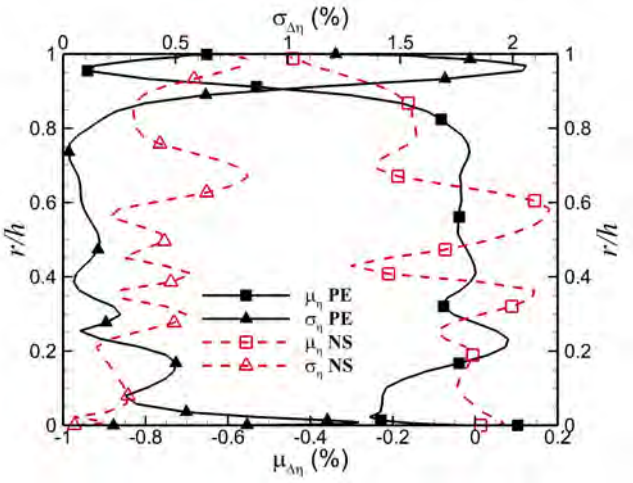

Figure 5 Outlet spanwise statistics of RVAE at PE and NS

The flow solutions of the 100 samples are firstly obtained by the same in-house program and then statistically analyzed. Figure 5 presents the spanwise distributions of statistics of RVAE at the outlet of Rotor 67. The mean performance exhibits significant degradations on the spans near hub and blade tip at PE, while it exhibits large degradations only on the spans near blade tip at NS. Meanwhile, the Stds are also the largest on the corresponding spans at PE and NS. On the middle spans, the variations of statistics are relatively smooth along span at PE, while there are zigzags along span at NS. As pointed out by open literatures (Luo et al., 2013; Strazisar et al., 1989), the flow separates from the suction side on the spans near hub and the shock/tip-leakage interaction is intensive for transonic compressor rotor blades. The previous study (Xia et al., 2019) suggested that the sensitivity of the flow to the uncertainties is responsible for the performance changes. Whether the peaks of statistics on the spans near hub and blade tip are resulted by the variations of flow separation and shock/tip-leakage interaction or not require further demonstration. Besides, the zigzags of statistics on the middle spans at NS require to be further discussed.

In the following, the statistical flow solutions on the blade-to-blade streamsurfaces of four different spans, 2%, 45%, 60% and 95% blade height are presented and compared. Figure 6 and Fig. 7 present the contours of relative Mach number (RMN), statistical mean and Std of RMN change at PE and NS, respectively. On the span of 2% blade height, the flow suffers severe separation on the rear portion, especially near the trailing edge (TE). Negative and positive variations of the statistical mean are illustrated at PE. In such cases, the separation is intensified, resulting in more flow losses and reduced adiabatic efficiency, as shown in Fig. 5. The same variations are illustrated on 45% span at NS. As shown in Fig. 5, the adiabatic efficiency degradation at NS reaches the peak on 45% span. The statistical Std has been widely used to measure the sensitivity of flow to the uncertainties. On 2% and 45% spans at PE and NS, the Std in the separation regime is highest in the passage, demonstrating that flow separation is indeed the most sensitive to IFAV on the inner spans. Besides, on 45% span, the flow on the front portion of suction side is supersonic, where the compression waves or weak shock waves exist and the Std is considerable.

On 60% span, there exists a shock wave on the suction side. The positive statistical mean at PE implies that the mean of RMN increases before the shock and the resultant flow loss also increases. That's why the adiabatic efficiency at PE decreases on 60% span. However, the statistical mean at NS illustrates that the RMN in the streamwise direction firstly decreases and than increases, demonstrating that the mean flow losses due to the shock wave on the suction side should decrease. Although the mean flow losses due to the separation near TE increase, the overall flow loss on 60% span decreases and the adiabatic efficiency also increases. Generally, the shock wave and flow separation on the middle spans are most sensitive to IFAV because the Std is highest on the spans.

On 95% span, the shock wave on the suction side is weakened and close to TE, resulting in flow separation in the regime near TE. Similar to those on 60% span, the mean of RMN increases before the shock at PE and the resultant flow losses increase. The shock induced flow separation is even more sensitive to IFAV than the shock itself because the Std in the separation regime is higher. At NS, the statistical mean of RMN first decreases and then increases near the shock.

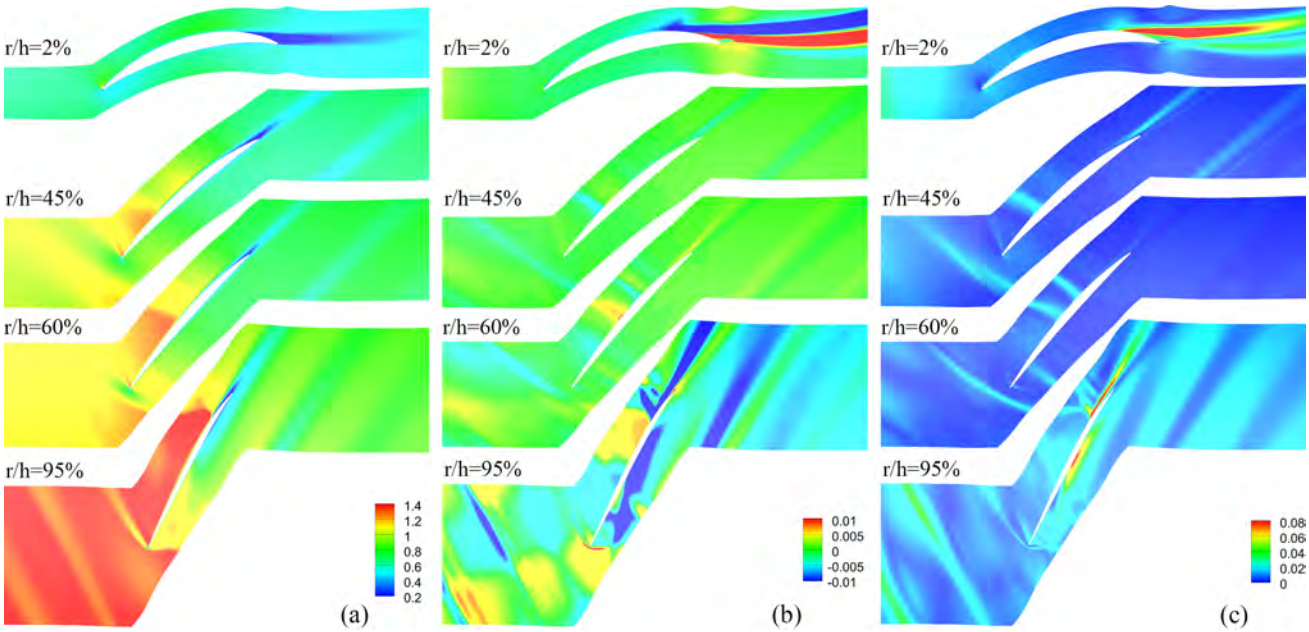

Figure 6 Contours on blade-to-blade streamsurface at PE: (a) nominal RMN; (b) statistical mean of RMN change; (c) statistical Std of RMN change.

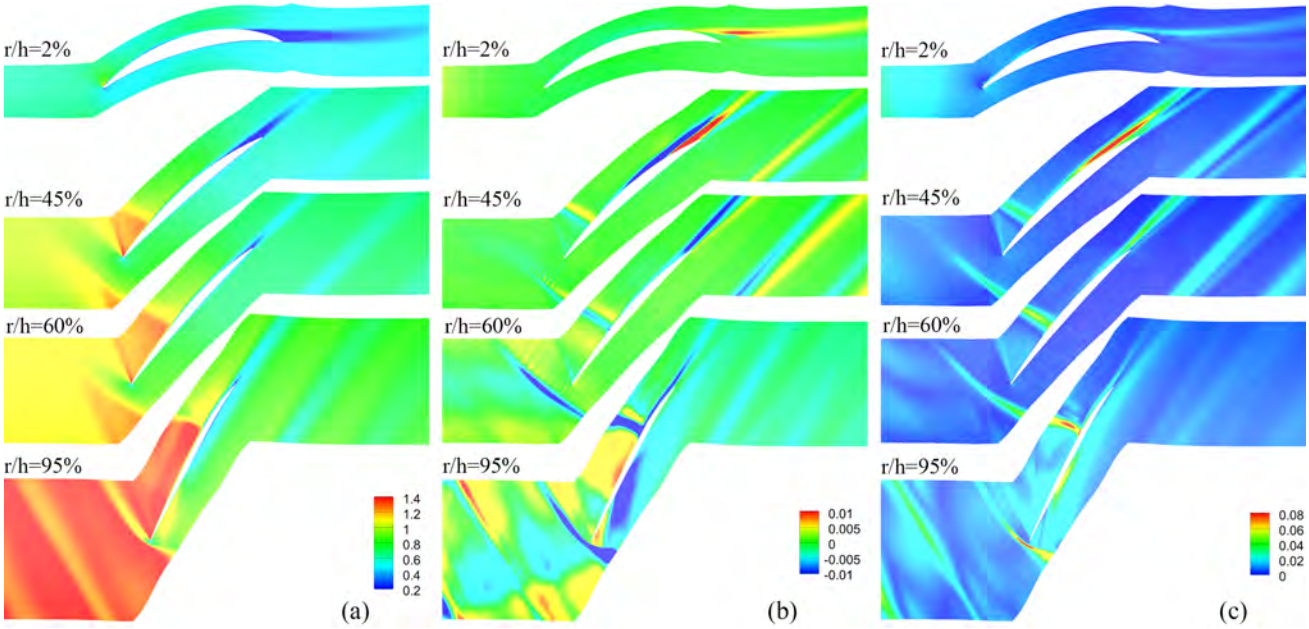

Figure 7 Contours on blade-to-blade streamsurface at NS: (a) nominal RMN; (b) statistical mean of RMN change; (c) statistical Std of RMN change.

In such cases, the adiabatic efficiency was supposed to increase. However, the mean RMN significantly decreases in the passage at both PE and NS, as shown by the contours of statistical mean of RMN change. It is well known that the tip-leakage flow originating from the pressure side plays the role as a jet entering the adjacent passage. The tip-leakage vortex stretches in both pithcwise and spanwise directions as moving downward along with the main flow. The effects of IFAV on the tip-leakage flow loss require to be studied.

The contours of statistics of vorticity on three different auxiliary planes are presented and compared. Figure 8 and Fig. 9 give the contours of vorticity, statistical mean and std of vorticity change at PE and NS. The normal directions of the auxiliary planes are the ones of local streamwise main flow, rather than the axial direction. It is well known that the vortices induced by tip-leakage flow mix with the streamwise main flow and gradually stretch in the passage. Through comparisons of the nominal vorticity it can be found that the tip-leakage vortex at NS is more intensive due to the higher loading.

On the auxiliary plane of 25% chord, the tip-leakage vortex concentrates near the casing. But the trend of radial penetration can be found, especially at NS. Along with the streamwise main flow, the tip-leakage vortex moves closer to the pressure side, as shown by the contours on the auxiliary planes of 50% and 75% chord. From the contours of Std of vorticity change it is known that the tip-leakage flow is another sensitive flow to IFAV. From the contours of statistical mean it is known that the mean vorticity is increased at PE and NS and more increments are obtained at PE, resulting in more flow loss. Moreover, It is interesting that the pitchwise penetration of tip-leakage vortex is strengthened when considering the effects of IFAV because the regimes with high statistics are closer to the pressure side by comparing with the nominal contours.

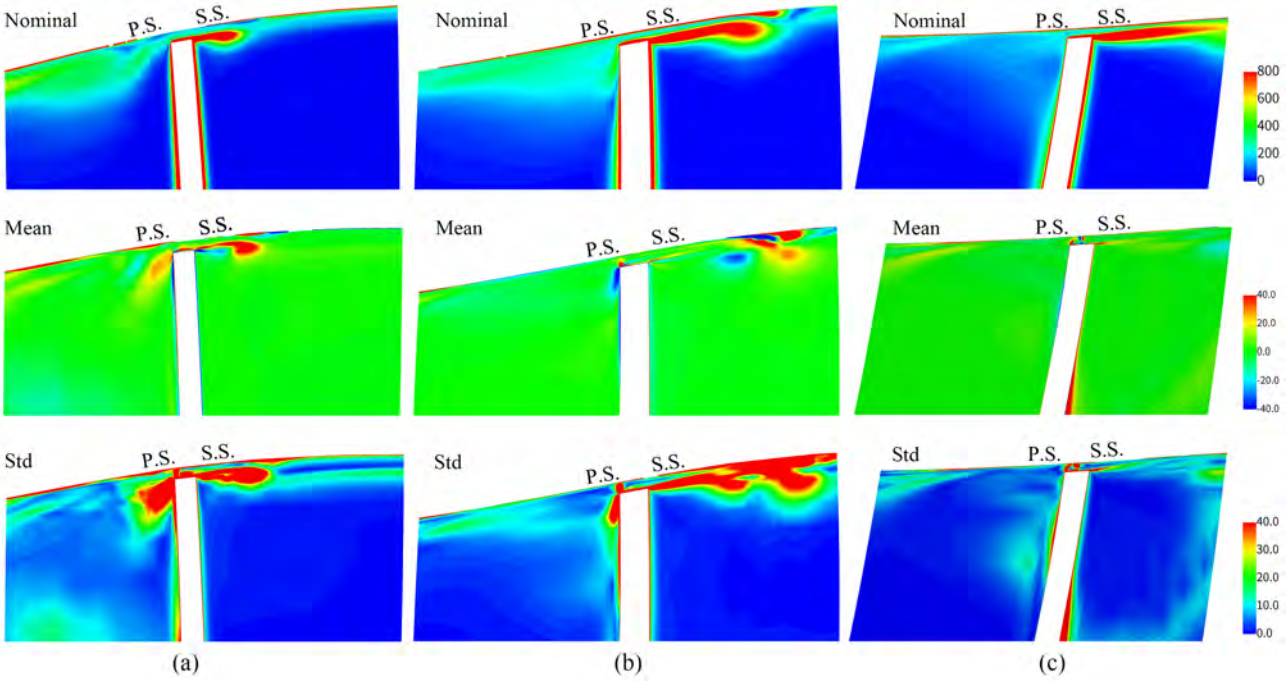

Figure 8 Contours of statistics of vorticity at PE: (a) 25% chord; (b) 50% chord; (c) 75% chord.

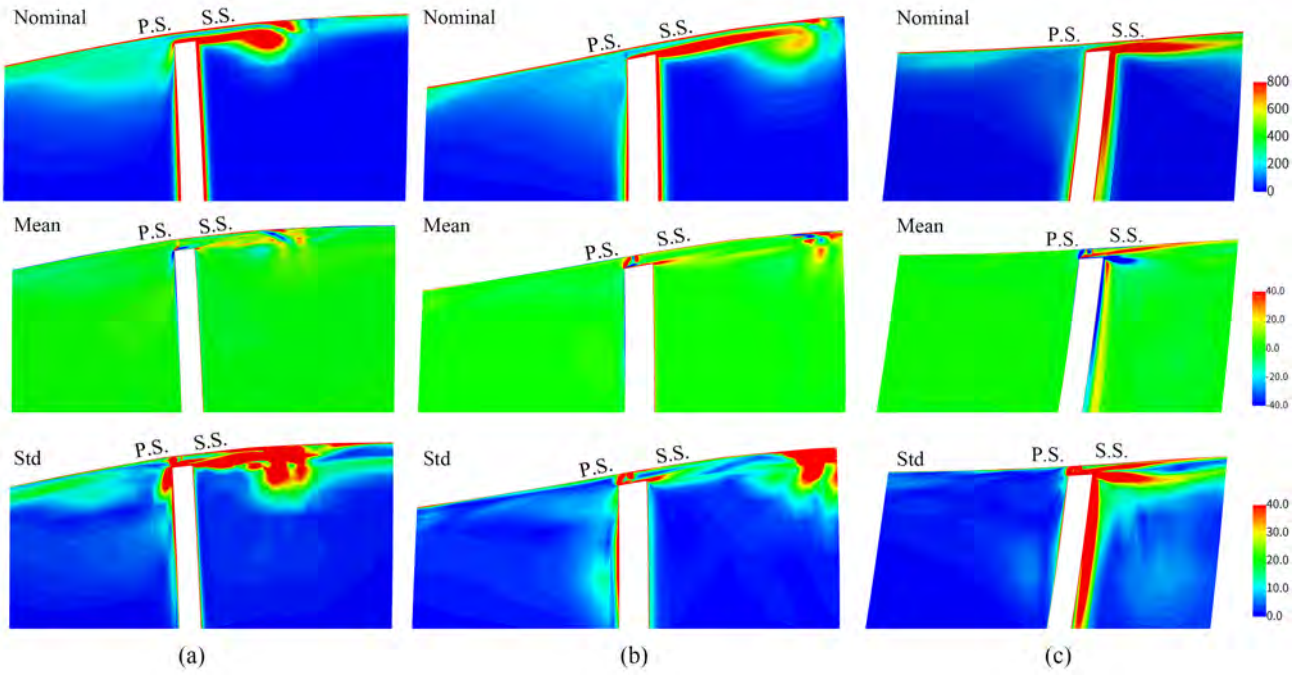

Figure 9 Contours of statistics of vorticity at NS: (a) 25% chord; (b) 50% chord; (c) 75% chord.

5. CONCLUSIONS

Grid-independent study assisted by Richardson extrapolation is introduced to validate the flow solutions of the transonic compressor rotor blade, Rotor 67 by solving RANS. Grid-independent solutions are obtained and the converged grid is used for performance impact of Rotor 67 considering the variations of inlet flow angle. The implementations of NIPC based on an adaptive sparse grid are introduced. Performance changes are then evaluated by NIPC at the operation conditions PE and NS. Finally, through statistical analysis of flow solutions base on the direct MCS, the impact mechanisms of IFAV are demonstrated.

(1) RVAE is nonlinear dependent on IFAV. The nonlinear impact intensifies as the range of IFAV increases, especially at the operation condition NS. Compared with the Gaussian distribution, IFAV agreeing uniform distribution has strengthened nonlinear impact on RVAE.

(2) The shock wave and flow separation on the suction side are sensitive to IFAV. On the inner spans, the variations of flow separation contribute most deteriorations of adiabatic efficiency. On the middle spans, the variations of flow separation near TE and shock wave on the suction side are responsible for the variations of adiabatic efficiency at the outlet. On the outer spans, besides the shock wave, the variations of tip-leakage vortex in the passage also contribute part of flow losses.

ACKNOWLEDGMENTS

The authors like to thank the National Natural Science Foundation of China (Grant nos. 51676003, 51976183) and National Science and Technology Major Project of China (Grant no. J2019-II-0012-0032) for supporting the research work.

References

Bammert, K. and Sandstede, H. (1976), 'Influences of manufacturing tolerances and surface roughness of blades on the performance of turbines', *Journal of Engineering for Power* **98**(1), 29–36.

Boyd, J. P. (1980), 'The rate of convergence of hermite function series', *Mathematics of Computation* **35**(152), 1309–1316.

Diakunchak, I. S. (1992), 'Performance deterioration in industrial gas turbines', *Journal of Engineering for Gas Turbines and Power* **114**(2), 161–168.

Edwards, R., Asghar, A., Woodason, R., LaViolette, M., Boulama, K. G. and Allan, W. D. E. (2011), 'Numerical investigation of the influence of real world blade profile variations on the aerodynamic performance of transonic nozzle guide vanes', *Journal of Turbomachinery* **134**(2). 021014.

Garzon, V. E. and Darmofal, D. L. (2003), 'Impact of geometric variability on axial compressor performance ', *Journal of Turbomachinery* **125**(4), 692–703.

Gerstner, T. and Griebel, M. (1998), 'Numerical integration using sparse grids', *Numerical Algorithms* **18**, 209.

Gopinathrao, N. P., Bagshaw, D., Mabilat, C. and Alizadeh, S. (2009), Non-deterministic cfd simulation of a transonic compressor rotor, *in* 'ASME Turbo Expo 2009: Power for Land, Sea, and Air', Vol. 6: Structures and Dynamics, Parts A and B, pp. 1125–1134.

Hosder, S., Walters, R. and Balch, M. (2007), Efficient sampling for non-intrusive polynomial chaos applications with multiple uncertain input variables, *in* '48th AIAA/ASME/ASCE/AHS/ASC Structures, Structural Dynamics, and Materials Conference', p. 1939.

Ju, Y. and Zhang, C. (2010), Multi-objective optimization design method for tandem compressor cascade at design and off design conditions, *in* 'ASME Turbo Expo 2010: Power for Land, Sea, and Air', Vol. 7: Turbomachinery, Parts A, B, and C, pp. 785–796.

Li, Z., Liu, Y. and Agarwal, R. K. (2018), Uncertainty quantification of geometric and flow variables affecting the performance of a transonic axial compressor, *in* '2018 AIAA Aerospace Sciences Meeting', p. 0068.

Loeven, A. and Bijl, H. (2010), The application of the probabilistic collocation method to a transonic axial flow compressor, *in* '51st AIAA/ASME/ASCE/AHS/ASC Structures, Structural Dynamics, and Materials Conference', p. 2923.

Loeven, G., Witteveen, J. and Bijl, H. (2007), Probabilistic collocation: an efficient non-intrusive approach for arbitrarily distributed parametric uncertainties, *in* '45th AIAA Aerospace Sciences Meeting and Exhibit', p. 317.

Luo, J. and Liu, F. (2018), Performance impact of manufacturing tolerances for a turbine blade using second order sensitivities, *in* 'ASME Turbo Expo 2018: Turbomachinery Technical Conference and Exposition', Vol. 2D: Turbomachinery, p. V02DT46A010.

Luo, J., Zhou, C. and Liu, F. (2013), 'Multipoint design optimization of a transonic compressor blade by using an adjoint method', *Journal of Turbomachinery* **136**(5). 051005.

Qin, R., Ju, Y., Wang, Y. and Zhang, C. (2016), Flow analysis and uncertainty quantification of a 2d compressor cascade with dirty blades, *in* 'ASME Turbo Expo 2016: Turbomachinery Technical Conference and Exposition', Vol. 2C: Turbomachinery, p. V02CT45A017.

Smolyak, S. A. (1963), 'Quadrature and interpolation formulas for tensor products of certain classes of functions', *Dokl. Akad. Nauk SSSR* **148**, 1042–1045.

Spalart, P. and Allmaras, S. (1992), A one-equation turbulence model for aerodynamic flows, *in* '30th Aerospace Sciences Meeting and Exhibit', p. 439.

Strazisar, A., Wood, J., Hathaway, M. and Suder, K. (1989), 'Laser anemometer measurements in a transonic axial-flow fan rotor'. NASA TP 2879.

Xia, Z., Luo, J. and Liu, F. (2019), 'Statistical evaluation of performance impact of flow variations for a transonic compressor rotor blade', *Energy* **189**, 116285.

Xiong, F., Xiong, Y., Greene, S., Chen, W. and Yang, S. (2009), A new sparse grid based method for uncertainty propagation, *in* 'ASME 2009 International Design Engineering Technical Conferences and Computers and Information in Engineering Conference', Vol. 5: 35th Design Automation Conference, Parts A and B, pp. 1205–1215.